

Sub-photospheric fluctuations in magnetized radiative envelopes: contribution from unstable magnetosonic waves

Koushik Sen^{1,2}, Rodrigo Fernández^{1*}, and Aristotle Socrates³

¹*Department of Physics, University of Alberta, Edmonton, AB T6G 2E1, Canada.*

²*Department of Physics, Indian Institute of Technology, Kharagpur, West Bengal, 721302, India.*

³*Jackson, WY 83001, USA.*

To be submitted to MNRAS

ABSTRACT

We examine the excitation of unstable magnetosonic waves in the radiative envelopes of intermediate- and high-mass stars with a magnetic field of $\sim \text{kG}$ strength. Wind clumping close to the star and microturbulence can often be accounted for when including small-scale, sub-photospheric density or velocity perturbations. Compressional waves – with wavelengths comparable to or shorter than the gas pressure scale height – can be destabilized by the radiative flux in optically-thick media when a magnetic field is present, in a process called the Radiation-Driven Magneto-Acoustic Instability (RMI). The instability does not require radiation or magnetic pressure to dominate over gas pressure, and acts independently of sub-surface convection zones. Here we evaluate the conditions for the RMI to operate on a grid of stellar models covering a mass range $3 - 40 M_{\odot}$ at solar metallicity. For a uniform 1 kG magnetic field, fast magnetosonic modes are unstable down to an optical depth of a few tens, while unstable slow modes extend beyond the depth of the iron convection zone. The qualitative behavior is robust to magnetic field strength variations by a factor of a few. When combining our findings with previous results for the saturation amplitude of the RMI, we predict velocity fluctuations in the range $\sim 0.1 - 10 \text{ km s}^{-1}$. These amplitudes are a monotonically increasing function of the ratio of radiation to gas pressure, or alternatively, of the zero-age main sequence mass.

Key words: instabilities – MHD – waves – stars: mass loss – stars: magnetic field – stars: massive

1 INTRODUCTION

Our understanding of stellar magnetism and mass loss in massive stars has evolved significantly during the last two decades. Spectropolarimetric surveys have shown that $\sim 7\%$ of O-type stars host persistent magnetic fields of $\sim \text{kG}$ strength (e.g., Wade et al. 2016; Grunhut et al. 2017). Similarly, about 10% of all A- and B-type stars are chemically peculiar and host surface magnetic fields $\gtrsim 300 \text{ G}$ (e.g., Landstreet et al. 2007; Aurière et al. 2007; Sikora et al. 2017). In addition to large-scale, stable fields, rapid variability in O- to A-type stars suggests that smaller-scale fields and fluctuations, presumably originating below the stellar surface, are present in a larger fraction of intermediate- and high-mass stars (e.g., Ramiaramanantsoa et al. 2014; Sudnik & Henrichs 2016; Sikora et al. 2017; Ramiaramanantsoa et al. 2018).

Mass loss in massive stars has also been subject to revi-

sion, with significant implications for massive star evolution (e.g., Smith 2014; Renzo et al. 2017). The smooth line-driven winds (Castor et al. 1975) that are often used in stellar evolution models are found to exceed observational estimates by factors of a few when clumping effects are taken into account (e.g., Najarro et al. 2011; Cohen et al. 2014). Clumping is expected from an intrinsic instability of line-driven winds (the *line deshadowing instability* or LDI; Lucy & Solomon 1970; MacGregor et al. 1979; Owocki & Rybicki 1984). Pervasive clumping is indeed found in time-dependent wind simulations that properly account for LDI effects (e.g., Owocki et al. 1988; Dessart & Owocki 2005; Sundqvist et al. 2017). However, agreement with observationally-inferred clumping factors is only obtained, particularly at the base of the wind, when an additional source of perturbations is assumed at the photosphere (Sundqvist & Owocki 2013).

Sub-photospheric fluctuations are most often assumed to be the consequence of wave excitation (primarily g-modes) by sub-surface convection zones at the iron opacity peak (Cantiello et al. 2009). The existence of this opacity

* E-mail: rafernan@ualberta.ca

peak is well established (Iglesias et al. 1992; Badnell et al. 2005), and the excitation of gravity waves at convective-radiative boundaries has been studied experimentally (e.g., Townsend 1966; Le Bars et al. 2015) and theoretically (e.g., Goldreich & Kumar 1990; Lecoanet & Quataert 2013). The effect of these convection zones is stronger with increasing luminosity and lower effective temperature (Cantiello et al. 2009). These convection zones could also be responsible for generating sub-surface magnetic fields via dynamo action (Cantiello & Braithwaite 2011) and thereby account for localized co-rotating magnetic structures.

Convection zones at the iron opacity peak disappear below a metallicity-dependent luminosity, however, and the presence of strong large-scale fields could even inhibit the development of these convection zones, since they are not very efficient while in the main sequence (Cantiello & Braithwaite 2011). Small-scale destabilization of purely acoustic waves is still possible for sufficiently strong radiative driving, if the opacity has the right density dependence (Blaes & Socrates 2003, hereafter BS03; Suárez-Madriral et al. 2013).

BS03 found that the presence of a magnetic field enables an additional source of small-scale (\lesssim gas pressure scale height), sub-photospheric fluctuations in stars with radiative envelopes. By performing a local linear stability analysis, BS03 identified the physical mechanisms involved and showed that the radiative flux can destabilize magnetosonic waves when the radiative force performs work on the wave velocity component along the background magnetic field. This instability had originally been identified in the context of highly-magnetized, radiation-dominated media (Prendergast & Spiegel 1973; Arons 1992; Klein et al. 1996) and the form of its non-linear development led to it being called the *photon bubble instability*. A number of studies have focused on the photon bubble instability in environments where radiation and magnetic pressure dominate over the gas pressure (Hsu et al. 1997; Gammie 1998; Blaes & Socrates 2001; Begelman 2001; Davis et al. 2004; Turner et al. 2005; Turner et al. 2007; Jiang et al. 2012). The instability mechanism is quite general, however, and it is predicted to occur even when the gas pressure dominates over both radiation and magnetic pressure, as is the case in the radiative envelopes of intermediate- and high-mass stars (BS03, Turner et al. 2004).

Fernández & Socrates (2013, hereafter FS13) studied the non-linear development of this instability over a wide range of conditions using local two-dimensional, time-dependent radiation-magnetohydrodynamic simulations in the diffusion regime. They confirmed the theoretical predictions of BS03 in that instability can occur even when the gas pressure is dominant. To better reflect the driving mechanism at wavelengths comparable or smaller than the gas pressure scale-height, they designated the process as the *radiation-driven magneto-acoustic instability* (RMI), given that no buoyancy is involved in this regime. The saturation amplitude of the RMI is a monotonic function of the ratio of radiation to gas pressure, and peaks when the magnetic pressure is comparable to the gas pressure. While FS13 pointed out the connection to sub-photospheric fluctuations in magnetized stellar envelopes, they did not apply their findings to realistic stellar models.

Here we set out to explore the importance of the RMI in the radiative envelopes of magnetized massive stars in which

radiation pressure has a moderate influence. We focus on stars for which the radiative flux is not too strong to generate a significant density inversion (which would significantly modify the background state; c.f. Jiang et al. 2015, 2017), nor too weak that the saturation amplitude becomes irrelevant. These conditions are also less favorable for the development of a significant sub-surface iron convection zone. We evaluate the RMI instability conditions on a grid of stellar evolution models, and estimate the magnitude of the density and velocity fluctuations expected based on the time-dependent simulation results of FS13. The goal is to map out the regions of parameter space in which the RMI is likely to play an important role in magnetized stellar envelopes.

The paper is organized as follows. Section 2 provides a brief overview of the RMI. Section 3 describes the stellar models and physical assumptions used. Results are presented in Section 4, followed by a summary and discussion in Section 5.

2 OVERVIEW OF THE RMI

In magnetohydrodynamics (MHD), the dispersion relation for magnetosonic modes is

$$\omega_0^2 = \frac{k^2}{2} \left[(c_s^2 + v_A^2) \pm \sqrt{(c_s^2 + v_A^2)^2 - 4c_s^2(\hat{k} \cdot \mathbf{v}_A)^2} \right] \quad (1)$$

where ω_0 is the mode frequency, k is the wave number and \hat{k} the unit wave vector, c_s is the sound speed, and $v_A = B/\sqrt{4\pi\rho}$ is the Alfvén speed, with B the magnitude of the magnetic field and ρ the fluid density. Positive and negative signs in equation (1) define the *fast* and *slow* magnetosonic branches, respectively, given the magnitude of the implied phase velocity $v_{ph} = \omega_0/k$. Magnetosonic modes reduce to sound waves in the limit of vanishing magnetic field.

BS03 showed that in a stably-stratified and optically-thick medium, magnetosonic modes with wavelengths shorter than the gas pressure scale height can be destabilized by a background radiation field when radiative diffusion is rapid compared to the mode frequency. The instability mechanism is quite general, and relies on the coupling of the wave displacement vector along the background magnetic field and the perturbation to the radiative flux, which results in work done on the fluid oscillation. Instability results when driving by the radiative flux overcomes damping from radiative diffusion. The instability operates under a broad range of conditions, including weakly-magnetized media in which radiation pressure is sub-dominant, such as in the envelopes of massive stars.

The condition that diffusion occurs more rapidly than the mode oscillation is

$$\omega_{diff} \equiv \frac{ck^2}{3\kappa_F\rho} \gg \omega_0, \quad (2)$$

where κ_F is the flux-mean opacity. This condition generally sets the maximum optical depth at which the RMI can operate. At small optical depth ($\tau \lesssim 1$) the driving mechanism becomes inefficient due to the weak coupling of matter and radiation.

In the outer layers of radiative envelopes, the timescale over which the fluid and radiation exchange energy is generally much shorter than the typical mode periods $\sim 1/\omega_0$. In

this case the fluid and radiation have the same temperature T , and in the limit of rapid diffusion, acoustic perturbations propagate at the isothermal sound speed

$$c_i^2 = \frac{p_{\text{gas}}}{\rho}, \quad (3)$$

where p_{gas} is the gas pressure (in this regime, c_i replaces c_s in equation 1). Quantitatively, the *thermal locking* condition can be expressed as

$$\omega_{\text{th}} \equiv \frac{4(\gamma - 1)E}{p_{\text{gas}}} \kappa_a \rho c \gg \omega_0, \quad (4)$$

where ω_{th} is a heat exchange frequency (BS03), $E = aT^4$ is the radiation energy density, a is the radiation constant, c is the speed of light, and κ_a is related to the Planck-mean and Thomson scattering opacities (§3.2).

Assuming rapid diffusion (equation 2) and thermal locking (equation 4), the approximate RMI instability condition for magnetosonic modes with wavelengths shorter than the gas pressure scale height is (BS03, FS13)

$$\zeta F \gtrsim \zeta^4 \left(p_{\text{gas}} + \frac{4}{3}E \right) c_i \quad [\text{slow modes}] \quad (5)$$

$$\zeta^2 F \gtrsim \frac{1}{\zeta} \left(p_{\text{gas}} + \frac{4}{3}E \right) v_A \quad [\text{fast modes}] \quad (6)$$

where F is the magnitude of the radiative flux \mathbf{F} ,

$$\zeta = \min \left(\frac{v_A}{c_i}, 1 \right), \quad (7)$$

and the two equations refer to the slow- and fast magnetosonic branches in equation (1). Equations (5)-(6) are obtained from the exact dispersion relation of BS03 by ignoring angular factors involving \mathbf{k} , \mathbf{B} , and \mathbf{F} . The two instability criteria demand that driving by the background radiative flux overcome damping by radiative diffusion. The factors of ζ are kept without simplification to show the dependence of driving and damping terms on the magnetic field strength. The growth rates are given by the difference between the left- and right hand sides times a global prefactor independent of magnetic field ($\sim \kappa_F / [c c_i]$).

An additional driving mechanism exists in the short-wavelength regime when the opacity has a density dependence. The instability criteria for fast and slow modes are (BS03)

$$\zeta^3 F \Theta_\rho \gtrsim \zeta^4 \left(\frac{4}{3}E + p_{\text{gas}} \right) c_i \quad [\text{slow modes}] \quad (8)$$

$$F \Theta_\rho \gtrsim \frac{1}{\zeta} \left(p_{\text{gas}} + \frac{4}{3}E \right) v_A \quad [\text{fast modes}], \quad (9)$$

where

$$\Theta_\rho = \frac{\partial \ln \kappa_F}{\partial \ln \rho} \bigg|_T. \quad (10)$$

Equations (8)-(9) quantify the relative importance of driving due to the radiative flux acting on opacity variations versus damping by radiative diffusion. As with the RMI instability criteria, the factors of ζ are not simplified so that driving and damping terms can be compared. The growth rates have the same global prefactor as the RMI-driven case. RMI dominates driving of slow and fast modes when $\zeta^{-2} \gtrsim \Theta_\rho$ and $\zeta^2 \gtrsim \Theta_\rho$, respectively. In the limit of vanishing magnetic field

($v_A \rightarrow 0$), the slow mode disappears, and the fast mode becomes a purely acoustic mode that can only be destabilized at small scales by the radiative flux if $\Theta_\rho \neq 0$ (BS03).

3 METHODS

3.1 Stellar Models

We generate a grid of stellar models using the stellar evolution code MESA version 6794 (Paxton et al. 2011, 2013, 2015, 2018). Since we are interested in stars with radiative envelopes with no density inversions, we choose an initial mass range $3 - 40 M_\odot$ and adopt solar metallicity. Rotation is ignored for simplicity. Models are considered up to the time at which they exhaust hydrogen at their centers, i.e., until the end of the main sequence. The choice is motivated by the fact that stars spend most of their time in this phase of evolution.

The quantities required to evaluate the instability criteria are taken directly from model profiles with the exception of the magnetic field, which is assumed and not included in computing the stellar structure (§3.3). We adopt three fiducial models with masses $6M_\odot$, $12M_\odot$, and $30M_\odot$ for further analysis, corresponding to stars that end their life in the Asymptotic Giant Branch, as a red-supergiant, and as a Wolf-Rayet star, respectively.

Most of the parameter choices for MESA models are the same as in Fernández et al. (2017): the *Dutch* wind model (de Jager et al. 1988; Nugis & Lamers 2000; Vink et al. 2001), and the overshoot choices of Fuller et al. (2015). We use the tabulated opacities (Type 1) from the OPAL library (Rogers & Iglesias 1992; Iglesias & Rogers 1996), and the ‘simple photosphere’ option for the atmospheric boundary condition (Paxton et al. 2011). The MESA `inlist` files and `run_star.extras.f` for the extraction of history columns are publicly available¹.

3.2 Opacity

The flux-mean opacity that enters the diffusion frequency (equation 2) is defined as (BS03)

$$\kappa_F F = \int_0^\infty d\nu \kappa_\nu^T F_\nu \quad (11)$$

where F_ν is the frequency-dependent flux, and

$$\kappa_\nu^T = \frac{1}{\rho} \left[\chi^{\text{th}}(\rho, T_g) + n_e \sigma_T \right] \quad (12)$$

is the total transport opacity, with χ^{th} the thermal absorption coefficient, T_g the gas temperature, n_e the electron density, and σ_T the Thomson scattering cross section.

In the diffusion approximation and in local thermodynamic equilibrium (LTE), the flux-mean opacity is equal to the Rosseland mean opacity κ_R if the flux depends only on the spatial gradient of the radiation energy density (e.g., Huebner & Barfield 2014). The assumption of LTE implies that each layer of the star is in radiative equilibrium, therefore diffusion of photons in energy space should be a secondary effect.

¹ https://bitbucket.org/rafernan/rmi_mesa_public

The absorption opacity κ_a that enters the thermal locking frequency ω_{th} is defined as (BS03)

$$\kappa_a = \kappa_P \left(1 + \frac{\partial \ln \kappa_P}{\partial \ln T} \right) + \frac{n_e \sigma_T}{\rho} \frac{kT}{m_e c^2}, \quad (13)$$

$$\simeq \kappa_P \left(1 + \frac{\partial \ln \kappa_P}{\partial \ln T} \right), \quad (14)$$

where m_e is the electron mass, k is Boltzmann's constant, and we have assumed local thermodynamic equilibrium. The second equality is valid when $kT \ll m_e c^2 \simeq 0.5$ MeV, as is the case in the envelopes of massive stars. The Planck-mean opacity is given by

$$\kappa_P = \frac{4\pi}{\rho a_\gamma c T^4} \int_0^\infty d\nu \chi^{\text{th}}(\rho, T) B_\nu(T). \quad (15)$$

This frequency average differs from κ_R in that (1) it excludes scattering contributions, (2) the weighting favors frequencies at which absorption is the largest instead of smallest, and (3) the weighting function peaks at a lower frequency for fixed temperature. Whenever absorption dominates over scattering, κ_P is thus larger than κ_R . This condition is safely satisfied in the radiative envelopes that are the subject of our study.

Given that MESA only outputs the Rosseland mean opacity and its derivatives, we compute the thermal locking frequency with κ_R instead of κ_P , which yields a lower-limit on ω_{th} when absorption dominates. To account for high-temperature regions in which scattering dominates over absorption, we subtract the Thomson scattering opacity from κ_R , and set

$$\kappa_a \simeq \kappa_R - (1 + X) \frac{\sigma_T}{2m_p}, \quad (16)$$

where X is the hydrogen mass fraction². Our results show that even with this conservative lower limit on ω_{th} , the regions that are unstable to the RMI are well into the thermally-locked regime.

While the value ω_{th} does not explicitly enter into the calculation of the instability criteria, it determines the scale below which modes thermally decouple and become adiabatic (BS03). The numerical results of FS13 showed however that in the non-linear phase of the RMI, most of the power is present at length scales comparable to the gas pressure scale height. We therefore ignore the dynamic range in wavelength over which the RMI operates, and consider *a posteriori* verification of equation (4) to be sufficient for the exploratory character of this work.

Finally, the density derivative of the flux-mean opacity Θ_ρ required to assess instability due to opacity variations (equations 8-9) is simply obtained from the density derivative of the Rosseland-mean opacity.

$$\Theta_\rho = \left. \frac{\partial \ln \kappa_R}{\partial \ln \rho} \right|_T. \quad (17)$$

² Equation (16) becomes negative in deep regions of the star for which scattering dominates, because the OPAL opacities include corrections to the Thomson cross section due to special relativity (Sampson 1959) and collective effects (Boercker 1987). While we could correct κ_a for these effects, the affected regions are deep enough in the star that RMI effects are not important, thus we ignore this artifact.

3.3 Magnetic Field and Instability Conditions

In order to evaluate the RMI instability criteria (equations 5-6) we need to assume a magnitude and direction for the magnetic field. For simplicity, we assume a constant background magnetic field inclined 45° relative to the outward radial direction. The fiducial magnitude is chosen as 1 kG following observed field strengths in O- to A-type stars (Grunhut et al. 2017; Sikora et al. 2017), and values of 0.3 and 3 kG are used to explore the sensitivity of results to this parameter. A spatially uniform magnetic field is a good first approximation to a large-scale field that varies slowly with depth in the outer envelope (\sim outermost solar radius).

It is also possible that sub-surface convection zones contribute to the generation of localized magnetic fields via dynamo action (e.g., Cantiello & Braithwaite 2011). In this case, the magnetic field strength depends on density as $B \propto \rho^{2/3}$ assuming that it rises buoyantly as a spherical blob, and is normalized such that it is in equipartition with the convective kinetic energy at the top of the iron convection zone. We include calculations that impose this spatial dependence of the field strength, in order to test the sensitivity of our results to the field geometry. *We note however that the instability conditions discussed in §2 assume a uniform magnetic field (BS03), and hence they are formally valid when $B/|dB/dr| \gg H_{\text{gas}}$, with $H_{\text{gas}} = p_{\text{gas}}/|dp_{\text{gas}}/dr|$ the gas pressure scale height.* Also, the mixing algorithms used to construct our stellar models ignore rotation and magnetic fields.

The presence of an instability is inferred when any of the left hand sides of equations (5)-(6) are larger than their respective right hand sides. Based on the results of FS03, we set $k = 1/H_{\text{gas}}$ in all calculations. The operation of any of these instabilities is contingent on the rapid diffusion condition (2) being satisfied, thus it is also evaluated. Finally, the condition of thermal locking (4) must be well satisfied for the validity of the equations used.

4 RESULTS

4.1 Instability regions for selected stars

The spatial locations of the RMI-unstable regions in the three fiducial models (6, 12, and $30M_\odot$ at solar metallicity) with spatially uniform magnetic field are shown in Figure 1. All three stars display the same qualitative features: (1) the outermost part of the envelope is unstable to both fast and slow magnetosonic waves, (2) the slow modes are unstable into deeper stellar layers than the fast modes, and (3) the instability regions overlap with the helium- and iron opacity peak convection zones.

The instability region for slow modes is set by the rapid diffusion condition (equation 2). This is partly a consequence of our assumption of constant magnetic field, which causes the ratio of magnetic to gas pressure $p_{\text{mag}}/p_{\text{gas}}$ to drop with increasing depth in the star [$p_{\text{mag}} = B^2/(8\pi) = \rho v_A^2/2$ is the magnetic pressure]. Damping due to radiative diffusion for this mode is suppressed relative to driving by a factor $(v_A/c_i)^3$ when $v_A < c_i$, thus radiative driving of this mode dominates throughout the star. When the rapid diffusion condition is no longer satisfied, however, magnetosonic modes become adiabatic and no driving occurs.

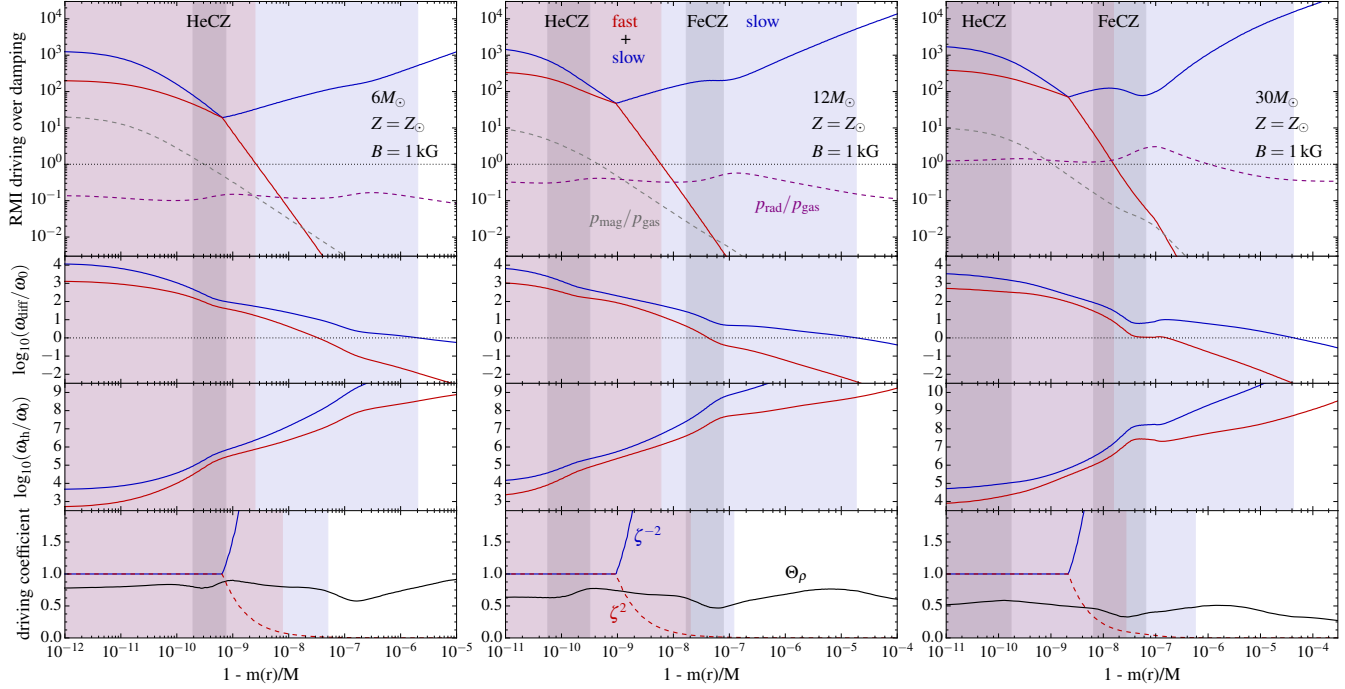


Figure 1. RMI instability regions as a function of fractional mass from the stellar surface, for 3 fiducial solar-metallicity models with masses $6M_{\odot}$ (left), $12M_{\odot}$ (center), and $30M_{\odot}$ (right), assuming a uniform magnetic field of 1 kG. The time is chosen to be 1/2 of the main sequence lifetime for each model (c.f. Figure 2). *Top row:* Ratio of RMI driving to damping terms (left over right sides of equations 5-6) for slow (solid blue) and fast (solid red) magnetosonic modes. The blue shaded area shows the region of the star in which only slow modes are unstable, whereas the red shaded area denotes zones where both slow and fast modes are unstable. The gray shaded areas correspond to convection zones driven by helium (left) and iron (right) opacity peaks. The purple and gray dashed lines show the ratios of radiation and magnetic to gas pressures, respectively. *Second row:* ratio of diffusion frequency to mode frequency for slow (blue) and fast (red) magnetosonic modes (equation 2). *Third row:* ratio of heat exchange frequency between gas and radiation to the mode frequency, for slow (blue) and fast (red) magnetosonic modes (equation 4). *Bottom row:* Coefficients that determine the relative importance of driving of short-wavelength modes by the RMI and by the radiative flux acting on opacity variations. The RMI dominates driving of slow and fast modes when $\zeta^{-2} \gtrsim \Theta_{\rho}$ and $\zeta^2 \gtrsim \Theta_{\rho}$, respectively, where ζ is given by equation (7) and Θ_{ρ} by equation (10). The shaded areas in this panel show the regions in which slow and fast modes are unstable to driving by opacity variations (equations 8-9).

Fast magnetosonic waves become unstable closer to the stellar surface than slow modes because damping by radiative diffusion is more efficient, and therefore a higher radiative forcing is required than for slow modes at the same depth. FS13 found that fast modes become unstable when a parameter measuring the diffusion speed c/τ_0 relative to the isothermal sound speed c_i exceeds unity

$$\mathfrak{R} = \frac{\ell_H}{4} \frac{c/c_i}{\tau_0} > 1 \quad (18)$$

where $\tau_0 = \kappa_F \rho H_g$ is the optical depth over a gas pressure scale height, and

$$\ell_H = \frac{H_{\text{gas}}}{H_{\text{rad}}} = \frac{p_{\text{gas}}}{p_{\text{rad}}} \left| \frac{dp_{\text{rad}}/dr}{dp_{\text{gas}}/dr} \right| \quad (19)$$

is the ratio of gas to radiation pressure scale heights (which is of order unity), with $p_{\text{rad}} = E/3$ the radiation pressure. The parameter \mathfrak{R} increases close to the stellar surface given that the isothermal sound speed and the density decrease sharply, and because the ratio of flux to radiation energy density

$$\frac{F}{Ec} \sim \frac{1}{\tau_0} \quad (20)$$

also increases. Because driving depends on the radiative flux

and damping on radiative diffusion and thus on E (equations 5-6), the ratio of F to Ec and thereby \mathfrak{R} quantify the amount of free-energy available to drive the RMI (BS03). Fast modes are therefore guaranteed to become unstable close enough to the photosphere. The fact that the RMI is valid in the diffusion approximation means, however, that there is a lower limit in optical depth to this instability region.

Figure 1 shows that in all models, both magnetosonic branches are well within the thermally coupled regime, with $\omega_{\text{th}} \gtrsim 10^3 \omega_0$ at the stellar surface. We therefore confirm *a posteriori* the validity of the instability equations used. The use of the Rosseland mean opacity in computing ω_{th} means that the real thermal coupling is likely to be much larger in regions where electron scattering does not dominate the opacity (§3.2).

Higher mass stars have a higher ratio of radiation to gas pressure throughout their interior. The larger importance of radiation pressure is associated with stronger radiative forcing of fast and slow modes for higher mass stars at any given point in the envelope, resulting in deeper instability regions for higher mass stars. Going from $6M_{\odot}$ to $30M_{\odot}$, the exterior mass unstable to slow modes increases from $\sim 10^{-6}$

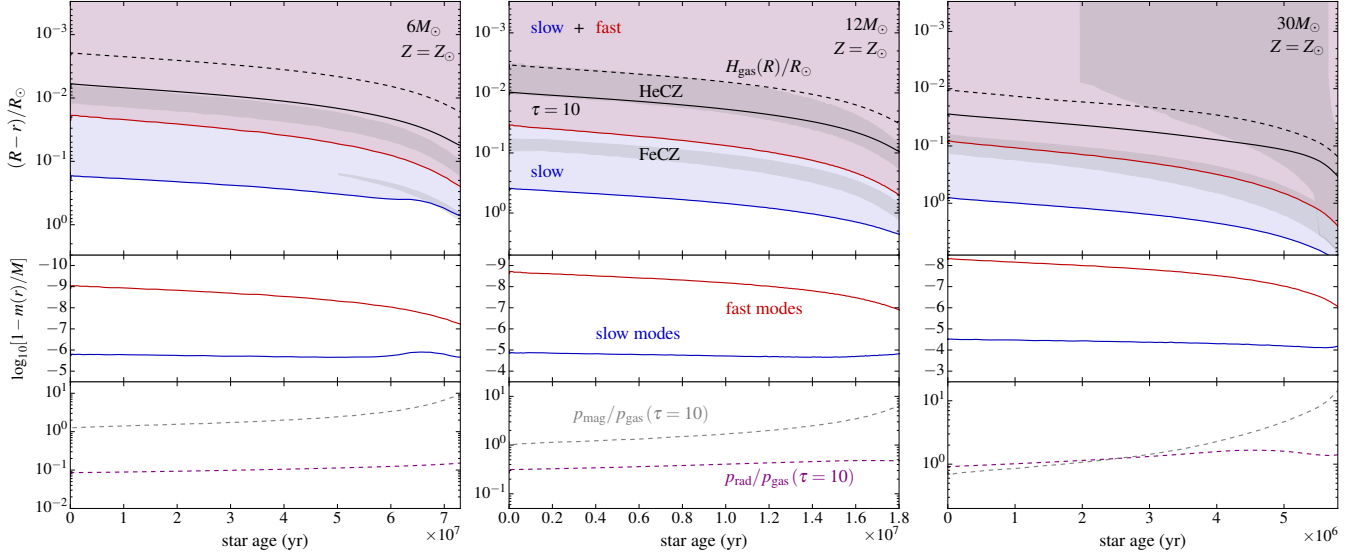


Figure 2. Instability regions as a function of time in the main sequence, for the three fiducial solar metallicity models ($6M_{\odot}$, $12M_{\odot}$, and $30M_{\odot}$) and a uniform magnetic field of 1 kG. *Top row:* depth below the stellar surface up to which only slow modes (blue curve) and fast plus slow modes are unstable (red curve). The gray shaded bands correspond to convection zones at the helium (top) and iron (bottom) opacity peaks. The black solid line denotes the radius at which the optical depth from the surface is $\tau = 10$, and the black dashed line shows the radius one gas pressure scale height from the surface. *Middle row:* Fractional mass from the stellar surface where slow modes (blue) and fast modes (red) become unstable. *Bottom row:* ratio of radiation to gas pressure (purple dashed) and magnetic to gas pressure (gray dashed) at the radius at which $\tau = 10$.

to almost 10^{-4} of the total stellar mass, while the fast modes affect the outermost $10^{-9} - 10^{-8}$ of the mass.

Figure 2 shows the evolution on the main sequence of the three fiducial models with constant magnetic field up to the time at which central hydrogen is exhausted. Over this period of time, stars expand in radius by a factor of a few, increasing in luminosity and decreasing in surface temperature. The instability regions move deeper in both radius and mass as the star evolves, approximately tracking surfaces of constant temperature, as shown by their relation to the convection zones at opacity peaks, which occur at specific temperatures.

The radial extent of the instability regions is also shown in Figure 2. Given that the RMI is valid in the optically thick regime, we adopt a fiducial value of the optical depth from the surface $\tau = 10$ as a conservative boundary of the region inside which the diffusion approximation is valid. Figure 2 shows that this radius lies a few gas pressure scale heights inside the stellar surface.

If the RMI is to serve as a source of sub-photospheric fluctuations, the place in the star where it is expected to be most prominent is where the free energy for the instability is the largest ($\mathcal{R} \gg 1$) while being simultaneously in the optically-thick regime, i.e., where the optical depth is not much larger than 1. The ratios of radiation to gas pressures and magnetic to gas pressures at $\tau = 10$ are shown in Figure 2. For a uniform field of 1 kG, magnetic and gas pressures are of the same order except near the end of the main sequence. The ratio of radiation to gas pressure does not depend strongly on depth and instead varies strongly with stellar mass.

In all 3 fiducial models with a uniform magnetic field, both fast and slow modes are unstable inside the radius where $\tau = 10$, and therefore can be considered to oper-

ate in the parameter regime where the RMI is valid and most effective. For fast modes, the spatial region involved ranges from a few percent to $\sim 10\%$ of a solar radius for the $6M_{\odot}$ model, to $0.1 - 2R_{\odot}$ for the $30M_{\odot}$ star. The region where slow modes are unstable is much larger, ranging from $\sim 0.1R_{\odot}$ at a minimum for the $6M_{\odot}$ to several solar radii at the end of the main sequence lifetime of the $30M_{\odot}$ star.

4.1.1 Instability regions for a radially-varying magnetic field

In order to explore how the instability regions depend on the amplitude and radial dependence of the magnetic field strength, we explore a scenario in which the field is generated by dynamo action in the iron convection zone. In this case, flux-freezing on buoyantly-rising blobs implies a field strength scaling $B \propto \rho^{2/3}$, and a normalization such that the magnetic energy density matches the kinetic energy density in the convection zone (Cantiello & Braithwaite 2011).

Figure 3 shows the instability regions with this field configuration, for the same fiducial models shown in Figure 1. The resulting fields at the surface are 20 G and 100 G for the $12M_{\odot}$ and $30M_{\odot}$ models, respectively. In the case of the $6M_{\odot}$ star, the convection zone is too weak to generate any interesting field so we arbitrarily impose a surface field of 10 G to compare with the other models.

The instability regions shrink in mass, approximately by a factor 10. Nevertheless, slow modes are still driven by the RMI to a depth comparable to that of the iron convection zone. Regarding driving strength, the slow mode growth rate is suppressed by a factor (v_A/c_i) when $v_A < c_i$. The smaller ratio of magnetic to gas pressure relative to the case of a slowly-varying \sim kG field means that the efficiency with

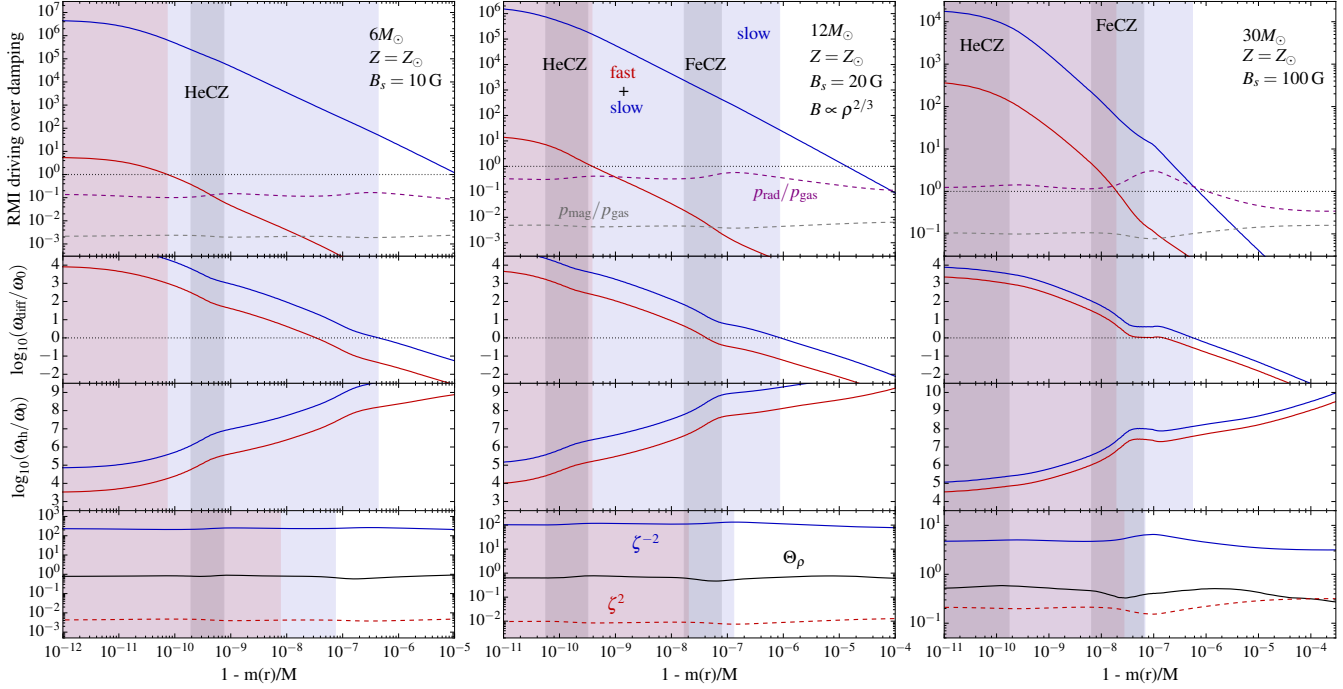


Figure 3. Same as Figure 1, but now assuming a magnetic field strength that scales with density as $B \propto \rho^{2/3}$, as appropriate for flux freezing in a buoyantly rising spherical blob. For the $12M_{\odot}$ and $30M_{\odot}$ models, the field is normalized so that the magnetic energy density is equal to the peak kinetic energy density in the iron convection zone (c.f. Cantiello & Braithwaite 2011). The resulting surface fields B_s are labeled in each panel. For the $6M_{\odot}$ star, the iron convection zone is non-existent or too weak when it appears later in the evolution, thus we simply impose a surface magnetic field of 10 G for comparison.

which energy from the radiation field is tapped by the RMI is low in this case.

While fast modes are technically unstable to the RMI to depths larger than $\tau = 10$ for the $12M_{\odot}$ and $30M_{\odot}$ stars, the driving is negligible compared to that due to the flux acting on opacity variations (4.1.2).

We emphasize again that the instability conditions derived by BS03 assume a spatially uniform magnetic field, and are therefore valid only on spatial scales comparable or smaller than the gas pressure scale height.

4.1.2 Relation between driving due to the RMI and density-dependent opacity

In the limit of small damping by radiative diffusion, the relative importance of the RMI and driving from opacity variations is given by the ratio of the terms on the left hand sides of equations (5)-(6) and (8)-(9), respectively for each mode. The RMI dominates the driving of slow modes if $\zeta^{-2} > \Theta_{\rho}$ and of fast modes if $\zeta^2 > \Theta_{\rho}$. Note that these conditions are independent of the ratio of radiation to gas pressure, since the flux scales out.

The bottom panel of Figure 1 shows these factors for the three fiducial models with uniform 1 kG magnetic field. In addition, the regions that are unstable to driving due to opacity variations (equations 8-9) are shown as shaded regions following the same color-coding as the RMI-driven regions in the panels above. Since at this field strength $p_{\text{mag}} \gtrsim p_{\text{gas}}$ at $\tau = 10$ for all three models, the ratio of driving terms is $\Theta_{\rho}^{-1} > 1$ and the RMI dominates over opacity fluctuations by a factor of a few. Moving inward in depth,

for a constant magnetic field, the importance of magnetic pressure relative to gas pressure decreases, and therefore ζ also decreases with depth.

Given the conditions in the envelopes of these fiducial models, RMI driving of slow modes always dominates over that due to opacity-variations. This condition is independent of the magnetic field strength, relying instead on the condition $\Theta_{\rho} < 1$, which is satisfied in all of our models (Figure 4) but can depend on other variables such as metallicity. The dominance of slow modes arises because driving by the flux acting on opacity variations has the same suppression factor $(v_A/c_i)^3$ as damping by radiative diffusion when $v_A < c_i$. This suppression factor is associated with the compressional component of the wave. Despite this dominance, the growth rate of slow modes is suppressed by a factor v_A/c_i in the limit of weak damping, therefore for a constant magnetic field, RMI activity should decrease with depth.

In the case of fast modes, RMI-driving becomes subdominant once $v_A/c_i \lesssim \Theta_{\rho}^{1/2}$. In this case, upward-propagating ($\hat{\mathbf{k}} \cdot \mathbf{F} > 0$) fast modes are driven by the flux acting on opacity variations, and downward going fast modes are damped (BS03). The instability region for fast modes driven by opacity variations is deeper than that due to the RMI, extending all the way to the top of the iron convection zone for the $12M_{\odot}$ and $30M_{\odot}$ models.

By setting a minimum optical depth at which the RMI can operate (given by the applicability of the diffusion approximation), the condition $v_A/c_i \geq \Theta_{\rho}^{1/2}$ sets a minimum magnetic field for which driving of fast modes is dominated

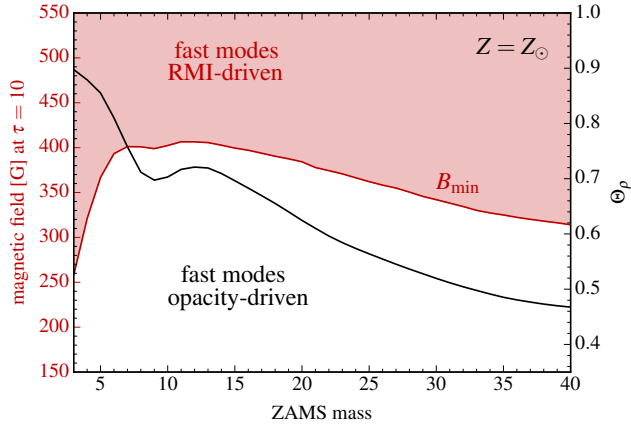


Figure 4. *Left:* minimum magnetic field for dominance of the RMI in driving of short-wavelength fast magnetosonic modes (equation 21, red curve) evaluated at $\tau = 10$, as a function of ZAMS mass for our grid of solar metallicity models. The time corresponds to that at which the central hydrogen abundance has decreased to one half of its initial value. *Right:* logarithmic opacity derivative (equation 10) at $\tau = 10$ for the same models at the same times.

by the RMI:

$$B_{\min} = (4\pi p_{\text{gas}} \Theta_{\rho})^{1/2} = \left(\frac{\Theta_{\rho}}{2}\right)^{1/2} B_{\text{eq}} \quad (21)$$

where $B_{\text{eq}} = \sqrt{8\pi p_{\text{gas}}}$ is the magnetic field that results in equipartition of magnetic pressure with gas pressure.

Figure 4 shows B_{\min} at $\tau = 10$ as a function of initial stellar mass for all our models. For a ZAMS $M < 6M_{\odot}$, this minimum field increases due to an increase in the stellar pressure near the surface. The field plateaus at about 400 G for stars in the mass range $6 - 15M_{\odot}$, subsequently decreasing at higher masses mostly due to a drop in Θ_{ρ} with increasing stellar mass. For fields significantly lower than ~ 300 G, fast magnetosonic modes are driven unstable primarily by the radiative flux acting on opacity variations, for all stellar masses.

The relative hierarchy of driving mechanisms in the weak magnetic field regime is illustrated in the bottom panel of Figure 3. Here, the condition $p_{\text{mag}} \ll p_{\text{gas}}$ results in $\zeta^2 \ll \Theta_{\rho} \ll \zeta^{-2}$, with slow modes driven by the RMI and fast modes driven by the flux acting on opacity variations. As in the strongly magnetized case, the region in which fast modes are driven by opacity variations extends all the way to the surface of the iron convection zone for the $12M_{\odot}$ and $30M_{\odot}$ models.

4.1.3 Metallicity effects

To investigate the effects of metallicity on the RMI, we evolve a $12M_{\odot}$ model with $Z = 10^{-2}Z_{\odot}$. During the main sequence, the model loses less mass than the solar metallicity model, has a smaller radius (by $\sim 50\%$) and higher effective temperature (by $\sim 30\%$) at all times. The iron convection zone is absent for most of the main sequence evolution, and the helium convection zone has a smaller convective Mach number than the solar metallicity model at a given age.

The unstable magnetosonic regions are qualitatively the

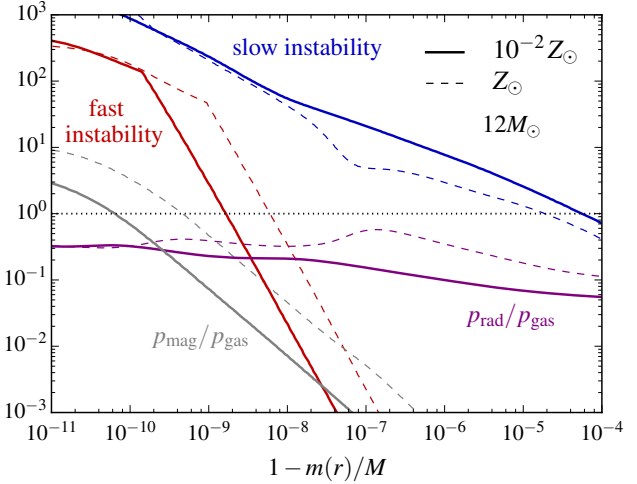


Figure 5. Profiles of RMI-related quantities for two $12M_{\odot}$ models, one with solar metallicity (dashed lines) and another with metallicity 10^{-2} times solar (solid lines). The time shown corresponds approximately to one half of the main sequence lifetime for each model. The ‘slow instability’ curve shows $\omega_{\text{diff}}/\omega_0$ for slow modes (equation 2), and ‘fast instability’ corresponds to the ratio of left to right hand sides of equation (6). Compare with Figure 1.

same as in the solar metallicity model, as shown in Figure 5. For a uniform 1 kG magnetic field and at a time equal to one half of the main sequence lifetime, the ratio of magnetic to gas pressure is smaller by a factor ~ 3 throughout the star compared to the solar metallicity model, while the ratio of radiation to gas pressure can be smaller by a factor up to ~ 2 . The region where slow modes are unstable extends to higher depths than in the solar metallicity model. This is expected for a lower opacity, which increases the diffusion frequency (equation 2). The region where fast modes are unstable extends to a shallower depth. This is consistent with stronger damping by radiative diffusion whenever $v_A < c_i$ (equation 6).

The values of the ratios $p_{\text{rad}}/p_{\text{gas}}$ and $p_{\text{mag}}/p_{\text{gas}}$ are comparable in both models, and therefore the instability operates in the same regime in both cases. We therefore do not expect the instability to be very sensitive to metallicity for the same background magnetic field.

4.2 Relation to convection zones from opacity peaks

Convection zones due to helium- and iron opacity peaks are ubiquitous in our stellar models, as shown in Figures 1-3. Both convection zones are completely contained by the region in which slow magnetosonic modes are unstable to the RMI, and the iron convection zone can sometimes overlap the region where fast modes are unstable to the RMI, as in the $30M_{\odot}$ model. It is therefore useful to clarify how these two very different sources of density fluctuations interplay with each other.

In a convectively unstable region, the relative importance of radiation diffusion and convection in transporting energy is determined by the convective efficiency. This efficiency can be quantified by the ratio of the isother-

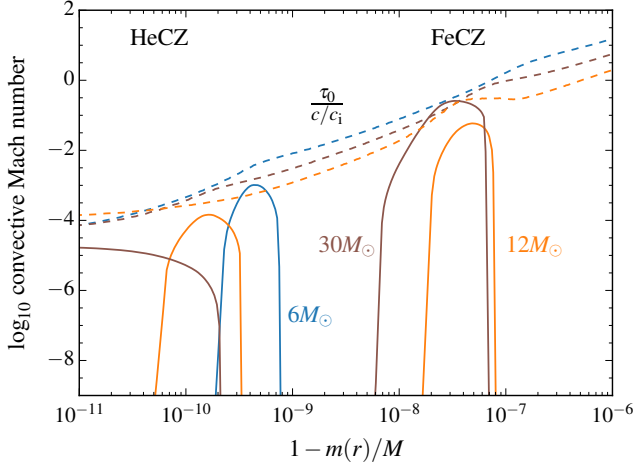


Figure 6. Convective Mach number at the time where the central hydrogen mass fraction is 0.35 for the three fiducial models (solid lines). Also shown as dashed lines is the convective efficiency parameter $\tau_0/(c/c_i)$, where τ_0 is the flux-mean optical depth over a gas pressure scale height.

mal sound speed c_i to the diffusion speed c/τ_0 . This ratio was found by Jiang et al. (2015) to correctly describe the regimes of high and low convective efficiency ($c_i \gg c/\tau_0$ and $c_i \ll c/\tau_0$, respectively) in radiation-hydrodynamic simulations of opacity-driven convection zones.

Figure 6 shows the convective Mach number in the opacity-driven convection zones halfway through the main-sequence time for our fiducial models (same times shown in Figure 1). As previously described by Cantiello et al. (2009), convective energy transport at the helium opacity peak is very inefficient, and can therefore be ignored. At the iron opacity peak, the convective Mach numbers are larger, and the efficiency is at most of the order of 10% at the end of the main sequence for the $30M_\odot$ star. The fraction of the stellar luminosity carried by this convection zone is at most a few percent in our models, although the Mach numbers can result in significant gravity wave excitation (the subsonic character of these convection zones make them less efficient at exciting acoustic waves directly; Cantiello et al. 2009).

We therefore consider an overall picture in which the iron convection zone excites gravity waves, as proposed by Cantiello et al. (2009), and the RMI excites compressional MHD waves in the radiative zone in between this convection zone and the photosphere (Figure 7). For stars at the low end of the mass range for radiative envelopes, the iron convection zone appears late in the main sequence (e.g., the $6M_\odot$ model in Figure 2), thus the RMI (or opacity variations at low magnetic field) may be the only source of small-scale sub-photospheric fluctuations. This could also be the case for stars at very low metallicity, for which iron convection zones are also weaker. For larger masses, and/or higher metallicities, convection zones become increasingly stronger and contribute with a larger energy flux in gravity waves. The interplay between the two mechanisms as a function of stellar mass is explored quantitatively in the following subsection.

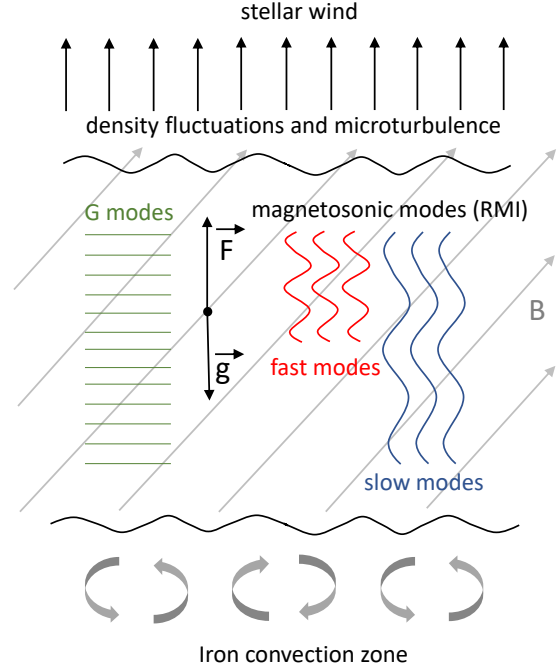


Figure 7. Schematic diagram of the operation of the RMI in massive star envelopes, with the vertical direction along the radial coordinate (\mathbf{g} is the acceleration of gravity and \mathbf{F} is the back-ground radiative flux). The star is radiative between the upper edge of the near-surface convection zone – driven by the iron opacity peak – and the photosphere. Compressional, short-wavelength MHD waves (slow and fast magnetosonic modes) are destabilized by the radiation flux in the radiative zone when a magnetic field \mathbf{B} is present. Since convection is subsonic, it is most effective at exciting gravity waves into the radiative layer. Perturbations from RMI-destabilized magnetosonic modes and convectively-excited gravity waves propagate toward the photosphere, providing a source of fluctuations that can result in microturbulence and wind clumping.

4.3 Dependence on stellar mass

Figure 8 shows the location of the RMI instability regions for slow- and fast modes as a function of initial stellar mass for all our models ($3 - 40M_\odot$) with a constant magnetic field of 1 kG. The age of the star is that at which the central hydrogen mass fraction decreases to 50% of its initial value.

The relative hierarchy of slow- and fast mode unstable regions is maintained for all models. The instability regions extend into deeper fractional mass and radii for more massive stars. The ratio of radiation to gas pressure at $\tau = 10$ is a monotonically increasing function of ZAMS mass, ranging from $p_{\text{rad}}/p_{\text{gas}} \simeq 0.04$ at $3M_\odot$ to $p_{\text{rad}}/p_{\text{gas}} \simeq 2$ at $40M_\odot$. The radiation pressure is at most comparable to the gas pressure. For the imposed magnetic field of 1 kG, the ratio of magnetic to gas pressure ranges from $p_{\text{mag}}/p_{\text{gas}} \simeq 7$ at $3M_\odot$ to $p_{\text{mag}}/p_{\text{gas}} \simeq 2$ at $40M_\odot$. In other words, the relevant sub-photospheric region is in the regime $p_{\text{mag}} \sim p_{\text{gas}}$, for which the RMI saturation amplitudes are maximized (FS13). Note however that as time elapses in the main sequence, the magnetic-to-gas pressure at $\tau = 10$ increases if the magnetic field is assumed to be constant (Figure 2).

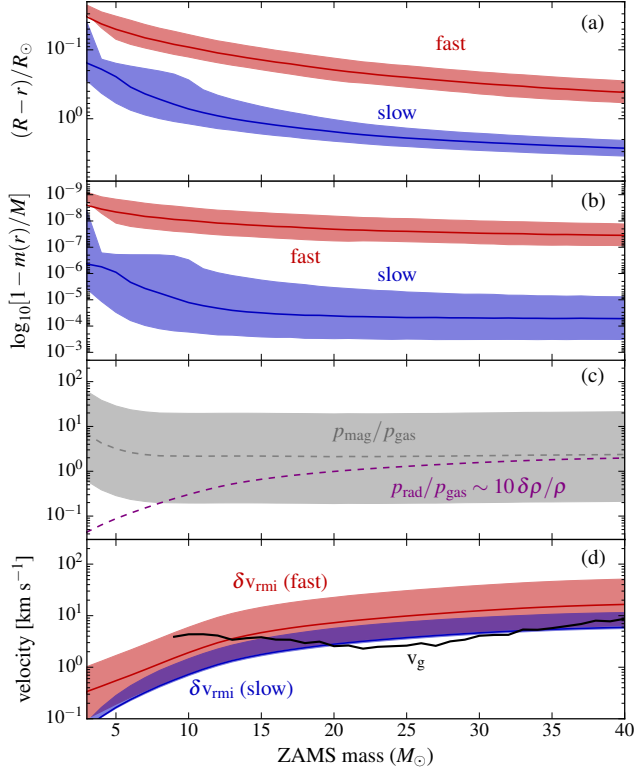


Figure 8. Properties of the RMI as a function of initial stellar mass, for solar metallicity models with a uniform 1 kG magnetic field. Shaded areas show the variation obtained for field strengths in the range 300 G to 3 kG. *Top:* Radial depth (in R_\odot) from the surface where fast (red) and slow (blue) magnetosonic modes are unstable. *Second panel:* Exterior mass unstable to the RMI, with fast and slow modes shown by the red and blue curve, respectively. *Third panel:* Ratio of radiation to gas pressure (purple) and magnetic to gas pressure (gray) at a radius where the optical depth from the surface is $\tau = 10$. For reference, the fractional density perturbations obtained in the simulations of FS13 satisfy approximately $\delta\rho/\rho \sim 0.1 p_{\text{rad}}/p_{\text{gas}}$ (equation 22). *Bottom:* Estimated velocity perturbation at $\tau = 10$ due to fast (red) and slow (blue) magnetosonic modes obtained from equation (23). For reference, we also show the estimated velocity perturbation at $\tau = 10$ from gravity waves excited by the iron convection zone (equation 25).

The simulations of the nonlinear development of the RMI by FS13 found saturation amplitudes that roughly satisfy:

$$\frac{\delta\rho}{\rho} \sim 0.1 \frac{p_{\text{rad}}}{p_{\text{gas}}} \quad (22)$$

for $p_{\text{rad}} \lesssim p_{\text{gas}}$, where $\delta\rho/\rho$ is the root-mean-square density fluctuation relative to the uniform initial background. Based on this expression we can relate the velocity perturbation associated with the RMI to the ratio of radiation to gas pressure. The velocity perturbation in the linear phase is (e.g. Appendix A of FS13)

$$\delta v_{\text{rmi}} \simeq v_{\text{ph}} \frac{\delta\rho}{\rho} \left[\frac{2v_{\text{ph}}^2 - c_i^2 - v_A^2}{v_{\text{ph}}^2 - (\hat{\mathbf{k}} \cdot \mathbf{v}_A)^2} \right]^{1/2} \quad (23)$$

The term in square brackets is of order unity except for slow modes in the limit $v_A \ll c_i$, in which case it becomes $(c_i/v_A)^2$, or ζ^{-2} . Given the moderate amplitudes implied by

equation (22), this expression is a reasonable first estimate for the velocity fluctuations induced by the RMI.

Figure 8 shows the magnitude of the RMI velocity perturbation at $\tau = 10$ obtained by evaluating equation (23) assuming a density amplitude as in equation (22). By construction, the amplitude of the perturbation is a monotonically increasing function of the ratio of radiation to gas pressure, which in turn is a monotonically increasing function of ZAMS mass. Fluctuations are larger for fast modes than for slow modes by a factor of a few, exceeding 1 km s^{-1} for $M \geq 7M_\odot$ and $M \geq 12M_\odot$ for fast and slow modes, respectively. At $M = 40M_\odot$, the amplitudes are 6 km s^{-1} and 17 km s^{-1} for slow and fast modes, respectively.

For comparison, we also compute the velocity fluctuation expected from gravity waves excited by the iron convection zone. The kinetic energy density in internal gravity waves near the stellar surface is estimated by Cantiello et al. (2009) as

$$E_g \sim \rho v_g^2 \sim \rho_c v_c^2 \mathcal{M}_c, \quad (24)$$

where v_g is the velocity associated with gravity waves near the stellar surface, ρ is the local density, and ρ_c , v_c and \mathcal{M}_c are the density, velocity, and Mach number near the top of the iron convection zone. Equation (24) assumes that the kinetic energy densities in the line formation region and at the top of the convection zones are comparable, because the volumes in these regions are similar and because the wave energy flux is conserved. The expression for the kinetic energy density of gravity waves at the top of the convection zone (Goldreich & Kumar 1990) is suitable for a discontinuous change in the Brunt-Väisälä frequency N^2 at the convective-radiative transition; a more detailed analysis taking into account the steep variation of this frequency with radius could yield a higher energy conversion efficiency (Lecoanet & Quataert 2013). Equation (24) results in a gravity wave velocity perturbation

$$v_g \sim v_c \sqrt{\frac{\rho_c}{\rho} \mathcal{M}_c}. \quad (25)$$

We compute ρ_c , v_c , and \mathcal{M}_c by averaging over the top 1.5 pressure scale heights of the iron convection zone, as done by Cantiello et al. (2009). We weight the average by the mass in each zone in the radial range.

The bottom panel of Figure 8 compares the estimated value of v_g from equation (25) with the velocity perturbation introduced by the RMI. Below $7M_\odot$, there is no iron convection zone operating in a significant way and the resulting (very small) gravity wave velocities are not shown. Over the range $7 - 40M_\odot$, the velocity fluctuations introduced by gravity waves excited by convection zones are comparable to those introduced by the RMI.

Figure 8 also shows the changes obtained in RMI-related quantities when varying the magnetic field strength from 300 G to 3 kG (without any feedback on the stellar structure). The ratio of magnetic to gas pressure varies by an order of magnitude in all models. The radial range of the fast and slow mode unstable regions change by a factor of order $\sim 10\%$, while the unstable mass can vary by up to an order of magnitude. Note that the variation of this regions is opposite for slow and fast modes: a stronger magnetic field increases the region unstable to fast modes.

This inverse dependence on field strength also trans-

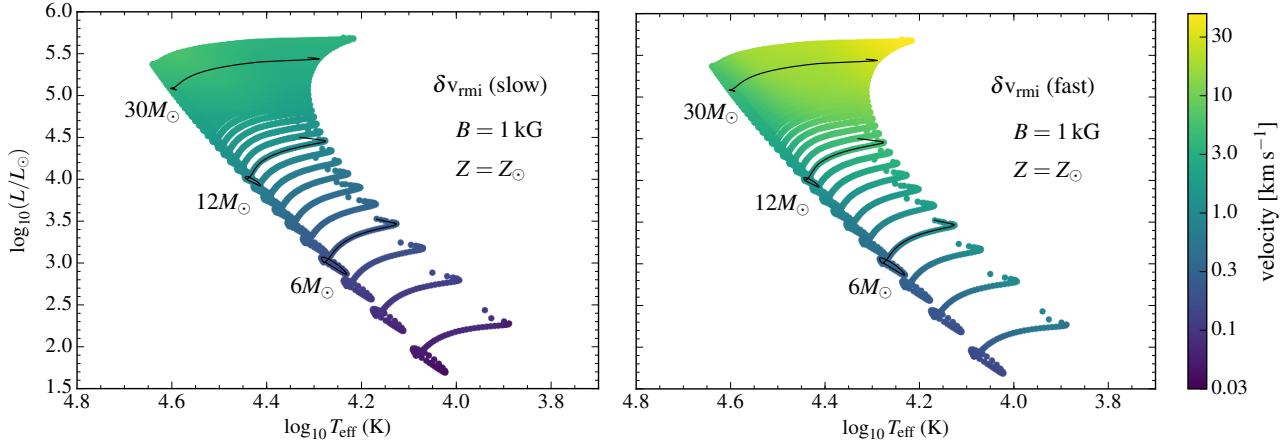


Figure 9. RMI-driven velocity perturbation at $\tau = 10$ on the H-R diagram, as estimated from equations (22)-(23), for all of our models, and assuming a uniform magnetic field of 1 kG. The left panel shows the slow mode and the right panel shows the fast mode. The thin black lines show the trajectories followed in the H-R diagram by our three fiducial models, as labeled.

lates to the velocity perturbation. The fast mode velocity perturbation increases monotonically with increasing magnetic field strength, while the slow mode velocity does not increase for $v_A > c_i$. For a weaker field, the slow mode velocity perturbation increases inversely with $(p_{\text{mag}}/p_{\text{gas}})^{1/2}$ due to the factor in square brackets in equation (23), which is inversely proportional to the compressional energy in the mode (FS13).

Figure 9 shows velocity perturbations due to slow- and fast modes driven by the RMI on an H-R diagram for all of our models, assuming a uniform magnetic field of 1 kG. The magnitude of the slow mode velocity perturbation does not vary significantly over the main sequence lifetime of each star, depending most strongly on stellar mass. The fast mode velocity perturbation increases with stellar age by up to about an order of magnitude from its value at the ZAMS, in addition to depending on the mass of the star.

Figure 9 suggests that the RMI can readily account for the microturbulent velocities discussed in Cantiello et al. (2009) (c.f. their Figure 9), in particular for stars below the luminosities (or metallicities) at which the iron convection zones disappear or become greatly weakened.

Variability timescales can be estimated by combining the value of the photospheric pressure scale heights with the velocities apparent in Figure 9. For the $3M_\odot$ star, the photospheric scale height ranges from $10^{-3} - 10^{-2}R_\odot$ from ZAMS to the end of the main sequence. RMI-induced velocities of $0.1 - 1 \text{ km s}^{-1}$, imply variability timescales ranging from tens of minutes to days. For our $40M_\odot$ star, both the scale heights and the velocity range are factor of about 10 larger, so the variability timescales should be similar. While the fastest growing mode of the RMI has wavelengths comparable to the gas pressure scale height, smaller wavelengths are also destabilized (BS03), with even shorter variability timescales being possible (FS13).

5 SUMMARY AND DISCUSSION

We have studied the conditions for the generation sub-photospheric fluctuations by unstable magnetosonic waves

in the radiative envelopes of intermediate- to high mass stars with a magnetic field. A grid of solar metallicity models covering the mass range $3 - 40M_\odot$ was used to evaluate the instability conditions for the Radiation-Driven Magneto-Acoustic Instability (RMI, also known as the photon bubble instability), in which slow- and fast magnetosonic modes are destabilized in optically-thick media by a background radiative flux when a magnetic field is present. Our main results are the following:

1. For a uniform magnetic field of $\sim 1 \text{ kG}$ strength, the RMI operates in all models we studied. Fast magnetosonic modes are unstable to a depth of a few pressure scale heights below the photosphere, while slow modes are unstable to depths beyond the iron convection zone (Figures 1 and 2).
2. Driving due to the radiative flux acting on opacity variations never dominates over the RMI for slow modes at short wavelengths, regardless of magnetic field strength or ratio of radiation to gas pressure, so long as $\Theta_\rho < 1$, as is the case in all of our models. For fast modes, driving due to opacity variations dominates for field strengths $\lesssim 300 \text{ G}$ (Figure 4, equation 21) or beyond the depth at which RMI driving of fast modes is stabilized by radiative diffusion (Figure 1).
3. Assuming that the magnetic field is generated at the iron convection zone results in fast modes being driven by the radiative flux acting on opacity variations (Figure 3). Slow modes are still driven by the RMI to similar depths as with larger field strengths, but with a smaller growth rate given the weak forcing when $v_A \ll c_i$ (equation 5).
4. The implied magnitude of velocity fluctuations for slow- and fast modes in the case of a $\sim 1 \text{ kG}$ spans from $\sim 0.1 - 10 \text{ km s}^{-1}$, with the amplitudes being a monotonically increasing function of the ratio of radiation to gas pressure, or alternatively, of the stellar mass (Figure 8 and 9). These amplitudes are comparable to those expected from the excitation of gravity waves at the top of the iron convection zone, whenever the latter is present. When

considering the RMI-driven velocities and the photospheric pressure scale height, the implied variability timescales range from minutes to days (§4.3).

5. Changing the magnetic field strength by a factor of a few does not alter our results qualitatively (Figure 8). The velocity amplitude of slow modes is a monotonically increasing function of the ratio of magnetic to gas pressure, while the amplitude of slow modes increases for smaller values of $p_{\text{mag}}/p_{\text{gas}}$.

6. Aside from significantly modifying sub-surface convection zones, lowering the metallicity results in minor quantitative modifications in the properties of the RMI, for a fixed background magnetic field (Figure 5).

The instability criteria studied in this paper are local, hence we cannot say anything about its effect on spatial scales larger than the gas pressure scale height. In particular, kinetic energy generated via the RMI can couple to global stellar oscillation modes, resulting in excitation of specific frequencies or in transfer of energy to other spatial scales. To assess these effects, global radiation-magnetohydrodynamic simulations of stellar envelopes are required.

Our velocity estimates are rough and subject to significant revision. In particular, the saturation amplitude of the RMI has never been studied in three spatial dimensions in the regime in which $p_{\text{rad}}, p_{\text{mag}} \lesssim p_{\text{gas}}$, as is applicable here. Use of equation (22) is therefore the best estimate we can make at the moment. Future work should address the saturation amplitude of this instability in all regimes of interest, using all spatial dimensions, and including realistic stellar opacities.

Similar uncertainties apply to the transition to the optically thin regime. At low enough optical depth, the conditions for the RMI to operate are no longer valid. Nevertheless, radiation can still impart significant momentum to matter – if only at specific wavelengths – thus interesting phenomena are likely to occur in the presence of a strong magnetic field. The development of suitable tools to study this problem will provide insight on this question.

ACKNOWLEDGEMENTS

We thank the referee, Steven Shore, for constructive comments that improved the manuscript. We also thank Huib Henrichs for stimulating discussions. KS was supported in part by the University of Alberta Research Experience (UARE) program and by the Inspire Fellowship Programme of the Indian Department of Science and Technology. RF acknowledges support from Natural Sciences and Engineering Research Council (NSERC) of Canada and from the Faculty of Science at the University of Alberta. This research was enabled in part by support provided by WestGrid (www.westgrid.ca) and Compute Canada (www.computeCanada.ca). Computations were performed at the *Jasper* and *Orcinus* compute clusters. This research also used storage resources (repository 2058) of the National Energy Research Scientific Computing Center (NERSC), which is supported by the Office of Science of the

U.S. Department of Energy under Contract No. DE-AC02-05CH11231.

REFERENCES

- Arons J., 1992, *ApJ*, 388, 561
Aurière M., et al., 2007, *A&A*, 475, 1053
Badnell N. R., Bautista M. A., Butler K., Delahaye F., Mendoza C., Palmeri P., Zeppen C. J., Seaton M. J., 2005, *MNRAS*, 360, 458
Begelman M. C., 2001, *ApJ*, 551, 897
Blaes O., Socrates A., 2001, *ApJ*, 553, 987
Blaes O., Socrates A., 2003, *ApJ*, 596, 509
Boercker D. B., 1987, *ApJ*, 316, L95
Cantiello M., Braithwaite J., 2011, *A&A*, 534, A140
Cantiello M., et al., 2009, *A&A*, 499, 279
Castor J. I., Abbott D. C., Klein R. I., 1975, *ApJ*, 195, 157
Cohen D. H., Wollman E. E., Leutenegger M. A., Sundqvist J. O., Fullerton A. W., Zsargó J., Owocki S. P., 2014, *MNRAS*, 439, 908
Davis S., Blaes O., Turner N., Socrates A., 2004, in Richards G. T., Hall P. B., eds, *AGN Physics with the Sloan Digital Sky Survey Vol. 311 of ASP Conference Series, Effects of Fluid Instabilities on Accretion Disk Spectra*. p. 135
de Jager C., Nieuwenhuijzen H., van der Hucht K. A., 1988, *A&AS*, 72, 259
Dessart L., Owocki S. P., 2005, *AAP*, 437, 657
Fernández R., Quataert E., Kashiyama K., Coughlin E. R., 2017, *MNRAS*, in press, arXiv:1710.01735
Fernández R., Socrates A., 2013, *ApJ*, 767, 144
Fuller J., Cantiello M., Lecoanet D., Quataert E., 2015, *ApJ*, 810, 101
Gammie C. F., 1998, *MNRAS*, 297, 929
Goldreich P., Kumar P., 1990, *ApJ*, 363, 694
Grunhut J. H., et al., 2017, *MNRAS*, 465, 2432
Hsu J. J. L., Arons J., Klein R. I., 1997, *ApJ*, 478, 663
Huebner W. F., Barfield W. D., 2014, *Opacity*, first edn. Springer, New York
Iglesias C. A., Rogers F. J., 1996, *ApJ*, 464, 943
Iglesias C. A., Rogers F. J., Wilson B. G., 1992, *ApJ*, 397, 717
Jiang Y.-F., Cantiello M., Bildsten L., Quataert E., Blaes O., 2015, *ApJ*, 813, 74
Jiang Y.-F., Cantiello M., Bildsten L., Quataert E., Blaes O., 2017, *ApJ*, 843, 68
Jiang Y.-F., Stone J. M., Davis S. W., 2012, *ApJS*, 199, 14
Klein R. I., Arons J., Jernigan G., Hsu J. J.-L., 1996, *ApJ*, 457, L85
Landstreet J. D., Bagnulo S., Andretta V., Fossati L., Mason E., Silaj J., Wade G. A., 2007, *A&A*, 470, 685
Le Bars M., Lecoanet D., Perrard S., Ribeiro A., Rodet L., Aurnou J. M., Le Gal P., 2015, *Fluid Dynamics Research*, 47, 045502
Lecoanet D., Quataert E., 2013, *MNRAS*, 430, 2363
Lucy L. B., Solomon P. M., 1970, *ApJ*, 159, 879
MacGregor K. B., Hartmann L., Raymond J. C., 1979, *ApJ*, 231, 514
Najarro F., Hanson M. M., Puls J., 2011, *AAP*, 535, A32
Nugis T., Lamers H. J. G. L. M., 2000, *A&A*, 360, 227
Owocki S. P., Castor J. I., Rybicki G. B., 1988, *ApJ*, 335, 914
Owocki S. P., Rybicki G. B., 1984, *ApJ*, 284, 337
Paxton B., Bildsten L., Dotter A., Herwig F., Lesaffre P., Timmes F., 2011, *ApJS*, 192, 3
Paxton B., et al., 2013, *ApJS*, 208, 4
Paxton B., et al., 2015, *ApJS*, 220, 15
Paxton B., et al., 2018, *ApJS*, 234, 34
Prendergast K. H., Spiegel E. A., 1973, *Comments on Astrophysics and Space Physics*, 5, 43

- Ramiamananantsoa T., et al., 2014, MNRAS, 441, 910
- Ramiamananantsoa T., et al., 2018, MNRAS, 473, 5532
- Renzo M., Ott C. D., Shore S. N., de Mink S. E., 2017, A&A, 603, A118
- Rogers F. J., Iglesias C. A., 1992, ApJS, 79, 507
- Sampson D. H., 1959, ApJ, 129, 734
- Sikora J., Wade G. A., Power J., 2017, preprint, arXiv:1712.02811
- Sikora J., Wade G. A., Rowe J., 2017, preprint, arXiv:1712.02821
- Smith N., 2014, ARAA, 52, 487
- Suárez-Madrigal A., Krumholz M., Ramirez-Ruiz E., 2013, preprint, arXiv:1304.2317
- Sudnik N. P., Henrichs H. F., 2016, A&A, 594, A56
- Sundqvist J. O., Owocki S. P., 2013, MNRAS, 428, 1837
- Sundqvist J. O., Owocki S. P., Puls J., 2017, A&A, submitted, arXiv:1710.07780
- Townsend A. A., 1966, Journal of Fluid Mechanics, 24, 307
- Turner N. J., Blaes O. M., Socrates A., Begelman M. C., Davis S. W., 2005, ApJ, 624, 267
- Turner N. J., Quataert E., Yorke H. W., 2007, ApJ, 662, 1052
- Turner N. J., Yorke H. W., Socrates A., Blaes O. M., 2004, RvMxAA, 22, 54
- Vink J. S., de Koter A., Lamers H. J. G. L. M., 2001, A&A, 369, 574
- Wade G. A., et al., 2016, MNRAS, 456, 2